Energy geotechnology: Implications of mixed fluid conditions

J. Carlos Santamarina & Jaewon Jang
School of Civil and Environmental Engineering, Georgia Institute of Technology, Atlanta, GA, USA, 30332

ABSTRACT: Multi phase fluids are common in energy-related geotechnical problems, including gas-water, gas-oil, ice-water, hydrate-water, and oil-water fluid conditions. The generalization of classical unsaturated soil mechanics concepts to energy geotechnology requires physical understanding of surface tension, contact angle, capillary pressure, solubility and nucleation. Eventually, these pore-level processes affect the granular skeleton. Together, pore and particle-scale interactions upscale through the sediment structure to affect its macroscale response. Possible emergent phenomena include fluid percolation, residual saturation and recovery efficiency; fluid driven fractures, lenses, fingering and pipe formation; bubble migration and bottom blow up.

1 INTRODUCTION

Energy geotechnology involves geotechnical phenomena and processes related to energy, from resource recovery to infrastructure and waste management. Energy resources include fossil fuels (90% of all primary sources - coal, petroleum, and gas), nuclear, hydroelectric, and other renewable sources (wind, geothermal, solar, tidal, biomas). The most critical energy-related waste storages include: CO_2 geological storage (from fossil fuels), fly ash (from coal), nuclear waste, and coal-mining waste.

Resource recovery, energy infrastructure and waste management often involve multi-phase fluid conditions (Table 1 – classical infrastructure related conditions are not addressed in this manuscript). The most relevant cases are:

- L-G: water-air, water-CO_2 and water-methane interfaces (as well as other biogenic and thermogenic gases). The liquid L has molecules of the gas in solution, and the gas contains molecules of the liquid.
- L_1-L_2: water-liquid CO_2 (geological C-storage), and water-oil (petroleum reservoirs). Both liquids include molecules of the other liquid in solution.
- L-I: water-ice and water-hydrate. Related analyses can often be interpreted as the "solid" ice or hydrate phase behaving as a high viscosity fluid.

The purpose of this manuscript is to extend fundamental concepts in unsaturated soil behavior to address mixed-fluid conditions in energy geotechnology. First, we explore interfacial processes at the atomic scale; then, we identify emergent phenomena that affect field-scale applications. Concepts presented in the following section capture the essential characteristics; references are provided for detailed information.

Table 1. Mixed fluid conditions in energy geotechnology

Fossil fuels (oil, coal, gas. Unconventional: coal-bed methane, shale-gas, tight-gas sandstone, CH_4 hydrates)	
Recovery	water(l), oil(l) CO_2(g), CO_2(l) CH_4(g), CH_4(h)
CO_2 storage	water(l), oil(l) CO_2(g), CO_2(l), CO_2(h) CH_4(h)
Nuclear	
Spent fuel storage	air/vapor(g), water(l)
Renewable: solar, wind, tidal	
Compressed air storage	air/vapor(g), water(l)
Renewable: bio, geothermal	
Production	steam(g), water(l)

Note: Mixed fluid conditions in infrastructure are not listed. Phases shown in parenthesis (g: gas, l: liquid, h: hydrate).

2 ATOMIC-SCALE PHENOMENA

Geotechnical implications of mixed-fluid conditions arise from interactions at the atomic scale where surface tension and contact angle are defined.

Interfaces are in a state of dynamic equilibrium: molecules are continuously jumping from one phase to

the other. The average residing time for a molecule at the surface of a liquid is in the order of 10^{-6} s (Shaw 1992).

Interfacial phenomena are understood at the atomic level. The van der Waals force is the result of Coulombian interactions (Fig. 1a) between atoms or molecules that experience instantaneous polarization. A dipole experiences orientation polarization next to an ion (Fig. 1b); this situation is extended to the mutually induced rotation of two interacting dipoles (Keesom – Fig. 1c). An atom experiences displacement of the electron cloud relative to the nucleus in the vicinity of a charge or ion (Fig. 1d). Furthermore, a dipole may polarize an otherwise non polar molecule (Debye – Fig. 1e), and two non polar molecules may become mutually polarized because the instantaneous position of electrons confers an atom or molecule with some instantaneous polarity even when the time-averaged polarity is zero (London dispersion – Fig. 1f). The resultant Coulombian force for the instantaneous charge configuration shows mutual attraction in all these cases. The van der Waals force includes Debye, Keesom and London contributions (Fig. 1c, 1e, & 1f). The atomic analysis of van der Waals interactions helps explain surface tension and contact angle.

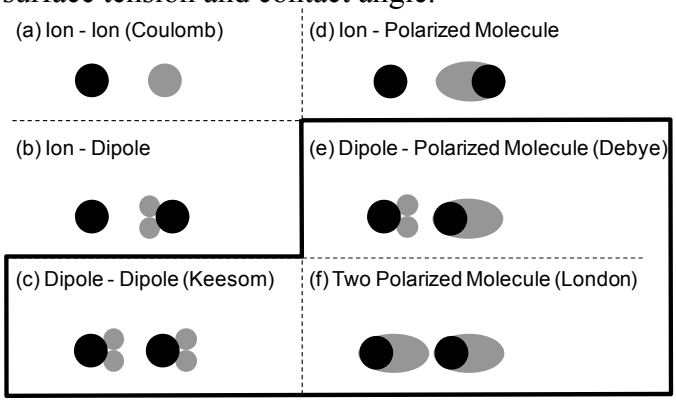

Figure 1. Electrical forces between ions and molecules. The van der Waals force combines Debye, Keesom and London contributions (Santamarina et al. 2001).

2.1 *Surface tension*

The time-average van der Waals attraction is isotropic when the molecule is away from the boundary. However, induced polarizations become anisotropic for molecules along the boundary and higher van der Waals attraction develops along the interface (Fig. 2). This situation alters the molecular organization in fluids near the interfaces. The altered molecular arrangement extends for about 5-to-10 mono-layers away from the interface. For example, water molecules at the water-vapor interface prefer to be oriented with their negative side towards the vapor phase, while random bulk conditions are attained at a distance of 1~2nm from the interface (Butt et al. 2006). Molecular dynamics simulations show the preferential alignment of water molecules near interface ions (Bhatt et al. 2004) and of water and CO_2 molecules at the interface (da Rocha et al. 2001, Kuznetsova & Kvamme 2002, Kvamme et al. 2007). These molecular-scale phenomena cause the emergence of a contractile membrane along the interface and a measureable surface tension T_s [mN/m]. This situation applies to L-G, L_1-L_2 and L-I interfaces.

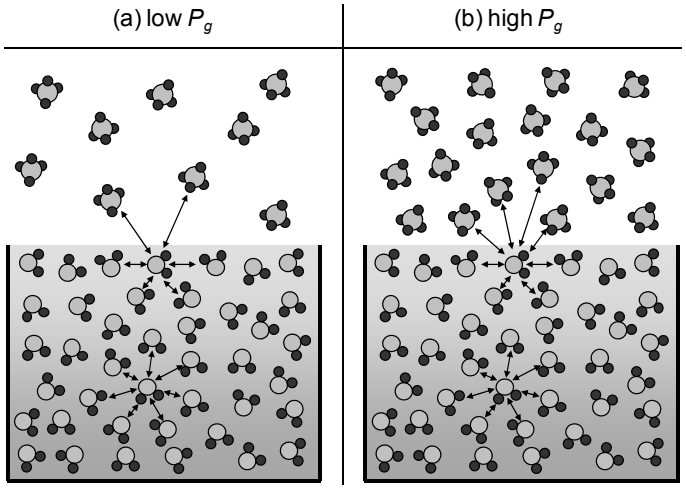

Figure 2. Effect of gas pressure on the development of surface tension along a gas-liquid interface. (a) Low gas pressure. (b) High gas pressure.

The effect of dissolved species. Foreign species modify the electrical field within the liquid and alter the interfacial tension. Solutes may either be repelled by the interface or attracted to it (van Oss et al. 2002). Variations in interfacial tension T_s [mN/m] with solute concentration c [mol/L] are anticipated in terms of surface excess of solute Γ [mol/m^2] (Butt et al. 2006, Pegram & Record 2007, Tuckermann 2007),

$$\left.\frac{\partial T_s}{\partial(\gamma c)}\right|_T = -\frac{RT}{\gamma c}\Gamma \qquad (1)$$

where γ [dimensionless] is the solute activity coefficient and T [K] is temperature. Ions are depleted at the interface $\Gamma < 0$ in inorganic solutions, but there is enrichment of organic species $\Gamma > 0$ at the interface when organic compounds are present. In the case of water-CO_2, there is high concentration of dissolved CO_2 near the interface, $\Gamma > 0$, causing a drop in interfacial tension (Chun & Wilkinson 1995, Massoudi & King 1974, Sutjiadi-Sia et al. 2008).

The effect of temperature. The balance between thermal activity and molecular forces determines the evolution of surface tension with temperature. In general, surface tension decreases with increasing temperature.

The effect of pressure: fluid density. Consider a liquid-gas LG interface. The proximity to and the number of near-neighbor charges depends on gas density. Hence, higher interaction and lower interfa-

cial tension is expected with increasing gas pressure and density (Sugden-Macleod equation T_s=f(Δρ) (Chun & Wilkinson 1995)). Likewise, the interaction with the external fluid remains relatively constant once the pressure exceeds the vapor-liquid boundary. Data for water-CO_2 in Figure 3 shows the pronounced sensitivity of interfacial tension with pressure and the relatively constant T_s values when pressure exceeds the CO_2 L-V boundary.

Critical point. A distinct separation between a liquid and its vapor ceases to exist and surface tension vanishes at *P-T* conditions above the critical point (Bauer & Patel 2009). The critical point for water is at 22MPa and 647K, and for CO_2 at and 7.4MPa and 304K. Supercritical fluid conditions develop above this pressure and temperature.

Values. Figure 3 and Table 2 show interfacial tension data for mixed fluid conditions relevant to energy geotechnology, including water-vapor, water-CO_2, water-CH_4, water-oil, water-ice, and water-hydrate.

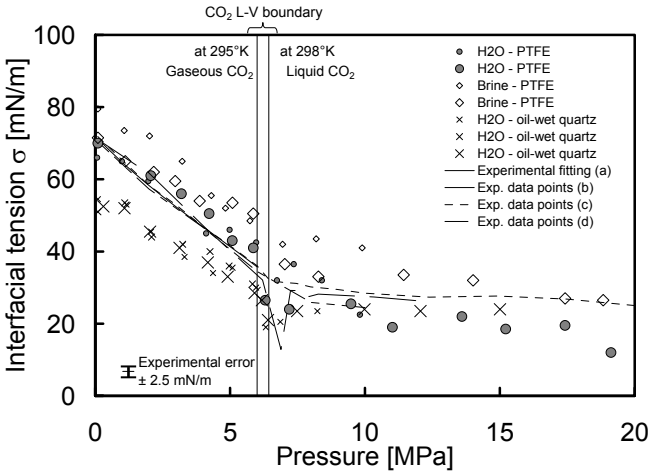

Figure 3. Interfacial tension between water and CO_2. Lines indicate values reported in the literature for deionized water at ~298K. Collected data and measured values reported in Espinoza & Santamarina (2010).

Table 2. Interfacial tension and contact angle.

	Interfacial tension [mN/m]	Contact angle [°]
Water-CO_2 (g)	72[a] (0.1MPa,298K)	38[a] on calcite (0.1MPa, 298K)
Water-CO_2 (l)	30[a] (7MPa, 298K)	30[a] on Calcite (7MPa, 298K)
Water-CH_4 (g)	72[b] (.1MPa, 298K) 64[b] (10MPa, 298K)	105[a] on PTFE (0.1MPa, 298K)
Water-Oil	33[c] H_2O-benzene 49[c] H_2O-mineral oil	98~180[d] on mineral (308-366K)
Water-Ice	32[e]	~0[f] (water on ice)
Water-CH_4 (h)	39[g] 32[e]	no data found
Water-CO_2 (h)	30[e]	no data found

a-Espinoza & Santamarina 2010, b-Ren et al. 2000, c-Kim & Burgess 2001, d-Treiber et al. 1972, e-Anderson et al. 2003, f-Knight 1971, g-Uchida et al. 1999.

2.2 *Contact angle*

The contact angle formed by two adjacent fluids resting on a mineral substrate reflects the mutual interactions between the three neighboring phases.

Contact angle and interfacial tension. Fluid-fluid and fluid-solid interfaces attempt to shrink because of the corresponding interfacial tensions. The contact angle θ reflects the equilibrium between these forces. In particular, if a liquid is surrounded by its own vapor, the relevant surface tensions are the vapor-solid T_{VS}, liquid-solid T_{LS}, and liquid-vapor T_{LV} tensions.

The contact angle is computed from the sum of forces parallel to the solid surface (Fig. 4; Adamson & Gast 1997)

$$\cos\theta = \frac{T_{VS} - T_{LS}}{T_{LV}} \qquad \text{Young's Equation} \qquad (2)$$

The crystal structure of minerals explains the different affinity for fluids. For example, when crystallization takes place in an aqueous environment, groups with water affinity develop on the surface, and the contact angle that water forms on the crystal is lower than the angle observed in the same mineral crystallized in air (Shaw 1992).

Oil-wet and water-wet mineral surfaces. The assessment of wettability from contact angle measurements is depicted in Figure 4. By convention, the contact angle is measured with respect to water. Usually, mineral surfaces in soils and rocks are hydrophilic and water-wet conditions prevail. The oil-wet condition may result when a water-repellent agent (for example, silicone) is absorbed onto the mineral surface. Chemisorption of organic matter on the mineral surfaces may also create a hydrophobic surface. However, since mineral surfaces are hydrophilic in nature, the oil-wet condition can be considered a temporary condition. Thus, given enough time, organic fluids tend to be displaced by water. In short-time processes, wettability has a significant effect on multiphase flow, such as during enhanced oil recovery (Morrow 1990).

Hysteresis. The effects of temperature, pressure, chemical composition, and pH on interfacial tension and wetting of solid surfaces can be investigated by means of contact angle measurements (see techniques in Shaw 1992, Dullien 1992, Kwok & Neumann 1999). The apparent simplicity in the determination of contact angle is misleading. In particular, there is hysteresis in the contact angle θ with respect to the direction of fluid motion. There are two possible causes for contact angle hysteresis (Adamson & Gast 1997, Extrand 1998). First, there is the effect of surface roughness, whereby the macroscopically observed angle differs from the contact angle at the

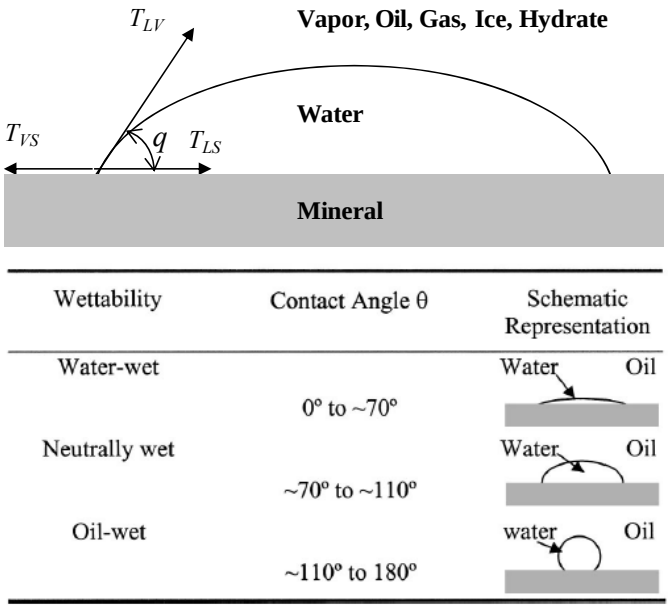

Figure 4. Wettability - Interfacial tension and contact angle. Ranges for water-wet, neutrally wet, or oil-wet surfaces. Note that water-wet or oil-wet conditions are established by testing the substrate with the two fluids present at the same time (from Francisca et al 2003)

scale of asperities, which is the scale relevant to Young's equation. Second, the contact angle is affected by surface heterogeneity due to the alteration of surface properties by fluids and the presence of surfactants or surface-active agents.

Pressure effects. Changes in interfacial tensions T_{VS}, T_{LS}, and T_{LV} (in particular) with pressure will alter the contact angle, particularly in liquid-gas-mineral systems such as water-CO_2-substrate and water-CH_4-substrate systems. For example, an increase in pressure from P=0.1MPa to ~8MPa causes an increase in contact angle of $\Delta\theta\approx45°$ (water on hydrophobized glass pressurized by CO_2), of $\Delta\theta\approx50°$ (Water droplet on Teflon-PTFE pressurized by CO_2), of $\Delta\theta\approx25°$ (CO_2 droplet on muscovite mica pressurized by brine), and of $\Delta\theta\approx60°$ (water on coal pressurized by CO_2) (Dickson et al. 2006, Siemons et al. 2006, Chiquet et al. 2007, Chi et al. 1988). Additional data are shown in Figure 5 for water-CO_2-mineral systems. Note that contact angle decreases on hydrophilic surfaces but increases on hydrophobic surfaces when T_{LV} decreases with increasing CO_2 pressure, as anticipated from force equilibrium analysis (Fig. 6). The CO_2-substrate interfacial tension is also affected by CO_2 pressure, and combines with changes in $T_{CO2\text{-}H2O}$ to fully explain results in Figure 5.

Values. Table 2 and Figure 5 provide contact angle data for mixed fluid conditions relevant to energy geotechnology, including water-vapor, water-CO_2, water-CH_4, water-oil, water-ice, and water-hydrate.

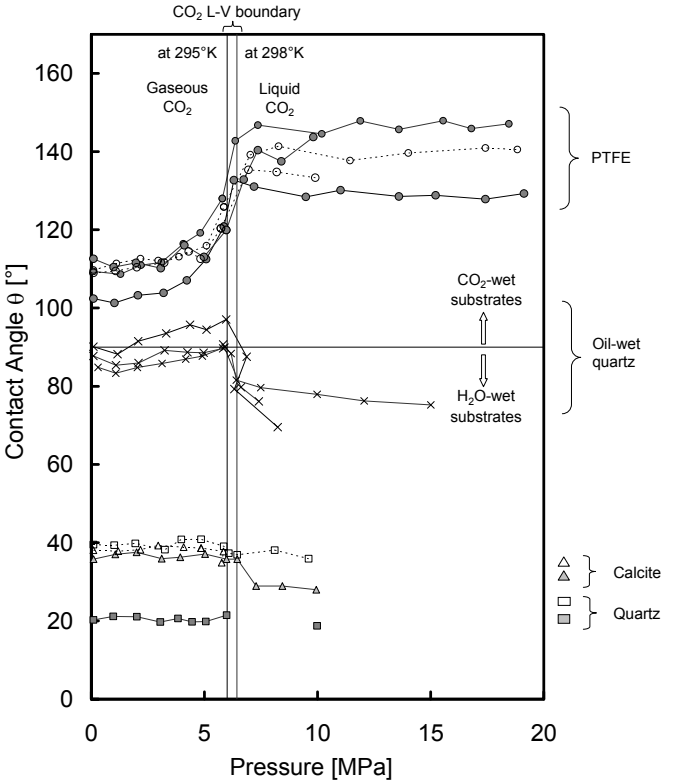

Figure 5. Contact angle evolution with pressure for a water droplet surrounded by CO_2 and resting on hydrophobic substrates (oil-wet quartz and PTFE) and hydrophilic substrates (quartz and calcite). Continuous lines: deionized water; dashed lines: brine (from Espinoza & Santamarina 2010).

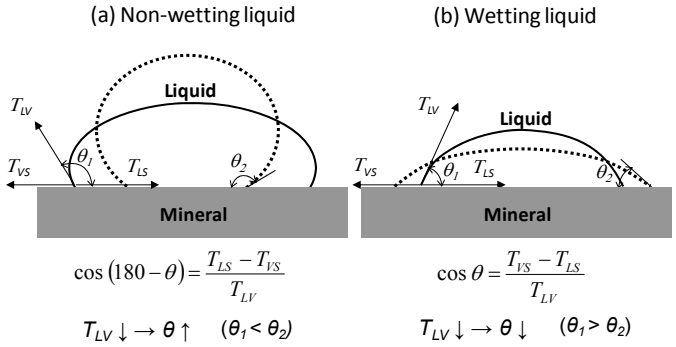

Figure 6. The effect of changes in interfacial tension on contact angle. The dotted line shows the droplet geometry when T_{LV} decreases.

2.3 *Capillarity*

Consider a water droplet surrounded by its vapor (Fig. 7a). The contractile interfacial membrane compresses the droplet increasing its internal pressure. The free body diagram shows that the difference between the internal liquid pressure and the external vapor pressure $\Delta u=u_L-u_V$ is related to the liquid-vapor interfacial tension T_{LV} as $\Delta u=2T_{LV}/R$ (Fig. 7a). More generally, the pressure difference between the two interacting fluids is related to the curvature of the interface:

$$\Delta u = T_{LV}\left(\frac{1}{R_1}+\frac{1}{R_2}\right) \qquad \text{Young-Laplace} \qquad (3)$$

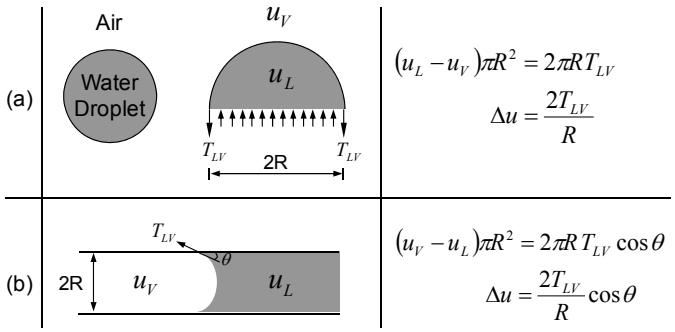

Figure 7. Fluid pressure and capillary phenomena as a function of interfacial tension and contact angle. (a) Water droplet. (b) Tube.

where R_1 and R_2 are the two principal radii of curvature. The same formulation permits computing the pressure difference between gas-water u_G-u_W, gas-oil u_G-u_O, ice-water u_I-u_W, hydrate-water u_H-u_W, and oil-water, u_O-u_W. Equation 3 anticipates that the pressure difference Δu can be large when small pores are involved. Implications on the development of discontinuities are explored later in this manuscript in the context of fractures and lenses. In a cylindrical pore, the pressure difference between the wetting and the non-wetting fluids is (Fig. 7b)

$$\Delta u = \frac{2T_{LV}}{R}\cos\theta \tag{4}$$

The vapor pressure is affected by the curvature of the liquid-vapor interface. Relative humidity and capillary pressure relate as (Defay & Prigogine 1966):

$$\Delta u = \frac{\rho}{M}\underline{R}T\ln\left(\frac{1}{h_r}\right) \tag{5}$$

where T is absolute temperature, $\underline{R}$ is the universal gas constant $\underline{R}$=8.31 N·m/mol·K, M is the molecular weight of the liquid, and ρ is the liquid density. Equilibrium in water-ice and water-hydrate systems is affected by temperature T (Clennel et al 1999, Coussy 2005, Coussy & Monteiro 2007, Gens 2010):

$$\Delta u = \Sigma_m\left(T_m - T\right) \tag{6}$$

where T_m is the melting temperature and Σ_m is the melting entropy (for ice: T_m=273.15K and Σ_m=1.2 MPa/K. We can combine these equations for the case of cylindrical tubes to obtain the size of pores invaded by the non-wetting phase at given relative humidity or temperature conditions:

$$R = \frac{2\,T_{LV}M\cos\theta}{\rho\underline{R}T\ln\left(\frac{1}{h_r}\right)} \qquad \text{water-vapor} \tag{7}$$

$$R = \frac{2\,T_{LV}\cos\theta}{\Sigma_m\left(T_m - T\right)} \qquad \text{ice or hydrate} \tag{8}$$

Equations 7 & 8 relate invaded pore size to either relative humidity or temperature, while Equations 3 & 4 relate pore size to capillary pressure. These equations together with pore structure (connectivity and spatial variability) define the characteristic curves Δu-S for the following systems under consideration: gas-water u_G-u_W, gas-oil u_G-u_O, ice-water u_I-u_W, hydrate-water u_H-u_W, and oil-water, u_O-u_W.

2.4 *Solubility – Saturation*

Phase A may dissolve or come out of solution from a neighboring phase B depending on pressure and temperature. During this process, interfaces may appear or disappear. When solubility limits for A-in-B and B-in-A are reached, an equal number of molecules from each specie travel from one phase to the other.

P-T dependent solubility. The *P-T* dependent concentration of a certain specie in another phase $M_{P,T}$ [mol/m^3] can be approximated using a linear function of pressure

$$M_{P,T} = P_{applied}\,k_H^0\cdot\exp\left[\frac{-\Delta H}{\underline{R}}\left(\frac{1}{T}-\frac{1}{T_{298.15K}}\right)\right] \tag{9}$$

The enthalpy of the solution is ΔH=-14130 [J/mol] for CH_4 in water, and ΔH=-19940 [J/mol] for CO_2 in water (Wilhelm et al. 1977). Typical values of Henry's constant for different gas species are listed in Table 3. Hence, the solubility of gas increases with increasing pressure and decreasing temperature, indicating an increased preference for dissolved gas rather than a separate phase at high pressure.

Table 3. Henry's law constants (data from Wilhelm et al. 1977)

Gas		Henry's constant k_H^0 [M/atm]
Carbon dioxide	CO_2	3.4×10^{-2}
Methane	CH_4	1.4×10^{-3}
Hydrogen	H_2	7.8×10^{-4}
Nitrogen	N_2	6.5×10^{-4}
Oxygen	O_2	1.3×10^{-3}
Sulfur dioxide	SO_2	1.2

Competing solutes. Solubility is affected by the emergence of new phases or the presence of competing solutes. For example, the presence of hydrates facilitates further hydrate formation and the equilibrium concentration of gas in water decreases in the presence of hydrate (Waite et al. 2009). Salt is a competing solute for dissolved gas and lowers the solubility of gas in water (Davie et al. 2004, Sun & Duan 2007, Tishchenko et al. 2005, Zatsepina & Buffett 1998).

Size-dependent solubility. Smaller water droplets in vapor, hydrate crystals in water, or gas bubbles in water have higher pressure, i.e., chemical potentials,

and require higher concentration (water or methane) in the surrounding fluid to balance that chemical potential (Henry et al. 1999, Kwon et al. 2008). This process is significant in small pores (e.g., smaller than ~40 nm for hydrate in seawater (Sun & Duan 2007).

Supersaturation. Solutions are often supersaturated at prevailing pressure and temperature conditions. The degree of supersaturation δ is defined as:

$$\delta = \frac{c_{actual}}{c_{equilib}} - 1 \quad (10)$$

Experimentally determined supersaturation values for different gases in water are listed in Table 4. The degree of supersaturation decreases if the solute nucleates as a separate phase and in the presence of certain impurities that facilitate (rather than hinder) nucleation.

Table 4. Measured values of supersaturation needed to cause bubble nucleation in aqueous solutions. Compiled from Lubetkin (2003).

Gas		Measured supersaturation
Carbon dioxide	CO_2	4.62~20
Methane	CH_4	80
Hydrogen	H_2	80~90
Nitrogen	N_2	19~140

2.5 *Nucleation*

Gas bubble formation, salt precipitation and hydrate nucleation phenomena are end-conditions to solubility. Critical nuclei size and heterogeneous nucleation play a critical role in the formation of a separate phase.

Heterogeneous nucleation. Supersaturation thresholds for homogeneous nucleation in the bulk liquid are a function of molecular interactions between the liquid and the dissolved gas. The presence of impurities and surface imperfections may facilitate nucleation and lower the degree of supersaturation. For example, the presence of mineral surfaces tends to favor heterogeneous bubble nucleation at substantially lower supersaturations. Nucleation centers in sediments include microcavities, irregularities and impurities at mineral surfaces (Dominguez et al. 2000, Blander 1979, Gerth & Hemmingsen 1980, Pease & Blinks 1947).

The heterogeneous nucleation of hydrate and ice on mineral surfaces is prompted by reduced thermal activity and spatial distribution of water molecules in the vicinity of mineral surfaces. However, ice or hydrate cages do necessarily form against the mineral surface as hydrogen bonding is needed to form the crystals. We can observe that: (1) the boundary layer may extend to few monolayers; (2) water molecules are not in a disordered liquid form, (3) water molecules have limited mobility, (4) diffusion through this layer is necessarily lower than in the bulk fluid, and (5) the hydrate (or ice) and mineral interface may sustain a tensile strength.

Critical nuclei size. Molecules continuously jump from one phase to the other, e.g., gas molecules jump from the bubble into the liquid and vice versa (numerical simulations in Walsh et al. 2009). The effect of size on solubility implies that molecules could jump out of small "embryos" faster than they could jump back into them. There is a critical nuclei size d^* for which nuclei are in equilibrium with the solution so that nuclei smaller than d^* will tend to dissolve (Nývlt et al. 1985, Finkelstein & Tamir 1985, La Mer 1952, Ward et al. 1970, Lubetkin 2003). Typically, stable nuclei are several nanometers in size and d^* decreases with supersaturation.

Ostwald ripening. The higher saturation predicted around smaller gas bubbles or crystalline nuclei promote diffusion from small nuclei towards large ones. Therefore a large bubble or crystal will tend to grow at the expense of smaller neighboring nuclei. This process is called Ostwald ripening. Ripening is a diffusion-controlled aging process and is important in fast crystallization processes that produce small crystal sizes. Ostwald ripening will alter the crystal size distribution with time (Myerson 2002).

Gas nucleation. Gas molecules occupy cavities between water molecules or between organic molecules in oil, until the fluid reaches the supersaturation threshold that prompts bubble nucleation (Ronen et al. 1989). Spontaneous bubble nucleation can result from: (1) depressurization of a pure liquid below the vapor pressure, (2) temperature increase for a pure liquid until the vapor becomes more stable than the pure liquid, (3) by gas coming out of solution from a supersaturated liquid (e.g., due to depressurization as per Henry's law; biogenic gas at constant pressure), or (4) by hydrate dissociation when *P-T* conditions migrate outside the stability field (Hemmingsen 1975 & 1977, Lubetkin 2003, Rebata-Landa & Santamarina 2010, Santamarina & Jang 2009).

Ice and hydrate nucleation. Ice forms at low temperature when the thermal activity of water molecules decreases to allow a solid structure. The presence of molecules such as CH_4 or CO_2 helps the nucleation of water cages around these gas molecules. The resulting crystalline structure is known as gas hydrate. Typical structures are shown in Figure 8a. The *P-T* phase boundaries for ice, CO_2 hydrate and CH_4 hydrate are shown in Figure 8b and c.

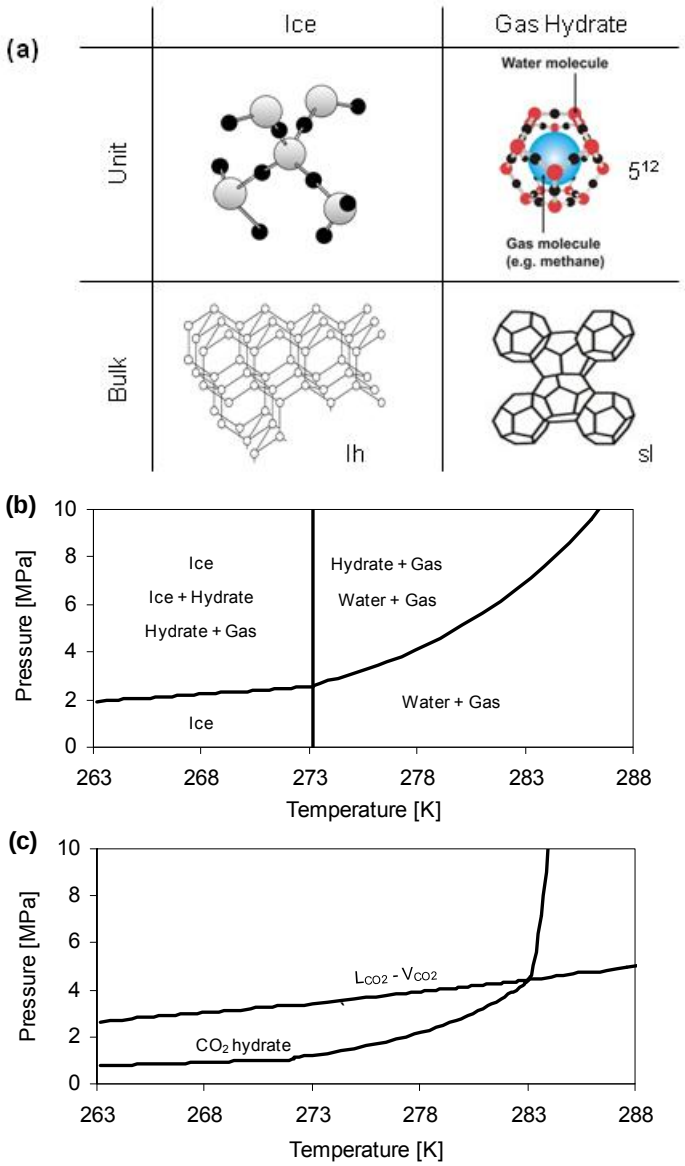

Figure 8. Ice and gas hydrate. (a) Molecular structure (figures from Sloan & Koh 2008 and Heriot-Watt University. (b) Phase boundary for methane hydrate. (c) Liquid-vapor and hydrate phase boundaries for carbon dioxide.

Ice and hydrates share similar properties. There are, however, two important differences. First, the phase boundary for ice is at almost constant temperature independently of pressure, while the phase boundary for CH_4 and CO_2 hydrates is pressure and temperature dependent. Differences in *P-T* phase boundaries define the location of permafrost (cold regions) versus the location of hydrates (offshore & below deep permafrost, i.e., high pressure & low temperature).

Second, water expands during ice formation; conversely, ice contracts as it melts (~8.3% volume contraction). The case of hydrates is more complex: the initial volume of water V_w increases to V_{hyd}=1.26V_w when methane hydrates form; upon dissociation, hydrates form water and gas phases and the initial volume of hydrate V_{hyd} expands to occupy a volume βV_{hyd} where β is *P-T* dependent: for *P*=10MPa and *T*=288.15K, β=2.26, the water occupies V_w=0.79V_{hyd} and the rest is the volume of gas V_g=1.47V_{hyd}. These pronounced volume expansion upon dissociation and the formation of separate gas and liquid phases anticipate significant implications of dissociation.

Gases and non-wetting fluids invade pores by displacing water, starting at large pores and gradually advancing into smaller pores, according to the interconnected pore structure. Ice and hydrate also invade the pore space along the larger-size interconnected porosity, but do so by crystallizing in pores.

3 PORE AND PARTICLE-SCALE ANALYSES

Interfacial tension, contact angle, solution / dissolution and formation / dissociation processes occur at the pore scale and affect the sediment response through particle-scale interactions. Related concepts and phenomena are analyzed next.

3.1 *Pores and pore throats*

Size – Statistics. The evolution of mixed-fluid phenomena in porous/granular media is intimately related to pore size distribution and spatial correlation.

The mean pore size $\mu(d_p)$ can be analytically estimated as a function of the void ratio *e*, the specific surface S_s [m^2/g] and the mineral density ρ [g/cm^3]

$$\mu(d_p) = k\frac{e}{S_s\,\rho} \tag{11}$$

where the shape factor is $k\approx5$ for spherical particles, k=2 for dispersed clays and k=4 for edge-to-face configuration. The void ratio depends on the effective stress σ' as

$$e = e_{1kPa} - C_c \log\left(\frac{\sigma'}{1kPa}\right) \tag{12}$$

where e_{1kPa} is the void ratio at σ'=1kPa and C_c the compressibility coefficient of the sediment.

We have compiled published pore size distribution data for clays, silts, and sands. Results show that pore size distribution statistics (mean and standard deviation) increase with particle size. When data are fitted with a log normal distribution, the standard deviation σ of ln(d_p/[μm]) is bound between (Phadnis & Santamarina 2010)

$$\sigma\left[\ln\left(\frac{d_p}{\mu m}\right)\right] = 0.4 \pm 0.2 \tag{13}$$

Finally, we note that pores are connected through pore throats. The size of pore throats is related to the size of the two connected pores; assuming a simple cubic configuration,

$$d_{th} \approx \frac{\sqrt{2}-1}{\sqrt{3}-1}\min\left(d_{p1}, d_{p2}\right) \sim 0.6\min\left(d_{p1}, d_{p2}\right) \quad (14)$$

Maximum capillary pressure. The pressure difference between the non-wetting and wetting phases $\Delta u_{\max}$ is limited by the largest pore throat along the boundary between wetting and non-wetting fluids

$$\Delta u_{\max} = u_{nw} - u_w \le \frac{4T_s}{\max\left(d_{th}\right)} \quad (15)$$

This pressure difference can develop in gas, oil, ice or hydrate phases in water-saturated sediments.

Upscaling – network models. Pore-scale phenomena upscale through the interconnected pore space. The interconnected porosity can be captured using tube-only, pore-only, and pore + tube network models. Tube-network models are used to compute flow conditions, assuming Poiseuille flow within each tube

$$q = \frac{\pi R_{tube}^4}{8\mu}\frac{\Delta P}{\Delta L} \quad (16)$$

where the flow rate through a tube q [m^3/s] is a function of fluid viscosity μ [N·s/m^2], tube radius R_{tube} [m], tube length ΔL [m], and pressure difference between end nodes ΔP [N/m^2]. These models allow us to study fluid flow even under mixed fluid flow conditions. On the other hand, pore-networks are better suited for the study of unsaturation; in this case, each pore is connected to its neighboring pores through throats that satisfy geometric constraints relative to the log-normal distributed pores. A comparative summary is presented in Figure 9.

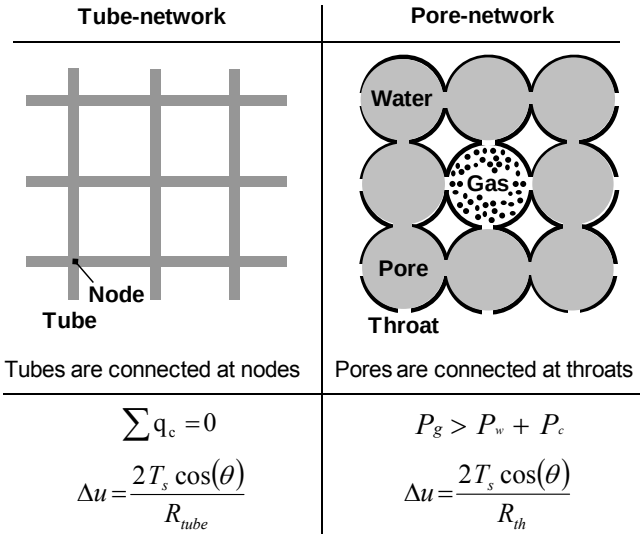

Figure 9. Networks of tube and of pores used for mixed fluid studies (details in Jang and Santamarina 2010a&b - See also Blunt 2001 for a comprehensive review of network models).

3.2 *Particle size – Particle level forces*

Sediments are particulate materials. Particle displacement, hence the macroscale sediment mechanical response, is determined by the forces particles experience. These include forces generated at the boundary and transmitted through the skeleton (i.e., due to effective stress), forces that result from the particle volume (weight and buoyancy), forces that develop along the particle surface (hydrodynamic and capillary) and contact level forces (electrical and cementation-reactive).

Asymptotic, order-of-magnitude estimates of the forces most relevant to this manuscript are summarized in Table 5. The normal contact force N related to the applied effective stress σ' scales with the square of the particle diameter $N=d^2\sigma'$ (assuming a simple cubic packing of equal size spheres). Weight and buoyancy combine to determine the submerged weight of a particle of unit weight γ_m submerged in a fluid of unit weight γ_f, $S=\pi(\gamma_m-\gamma_f)d^3/6$.

Table 5. Particle-level forces

Skeletal	$N=\sigma' d^2$
Weight	$W=\pi G_s\gamma_w d^3/6$
Buoyant	$U=\pi\Delta\gamma d^3/6$
Hydrodynamic	$F_d=3\pi\mu v d$
Capillary	$F_c=2\pi T_s d$
Electrical Attraction	$\text{Att}=A_h d/24t^2$
Electrical Repulsion	$\text{Rep}=0.0024c_0^{0.5}\exp(-10^8 t c_0^{0.5})d$
Cementation	$T=\pi\sigma_{ten} t d$

Re.: Cho et al (2001), Santamarina (2001); Gili&Alonso 2002

The capillary force a particle experiences when the sediment is subjected to mixed fluid conditions can be estimated using sketches shown in Figure 10 (Note: this analysis applies to vapor-water, gas-oil, oil-water, ice-water and hydrate-water mixtures). There are two force components. One is exerted by the interfacial membrane in the direction of the wetting fluid, as the interfacial membrane clings to the mineral around the grain surface. The second component is caused by the pressure difference between the wetting and the non-wetting phase against the cross section of the grain. Then, the capillary force acting on the grain and transmitted to the sediment skeleton is (compressive towards the side of the wetting fluid)

$$F_{cap} = \pi d T_s\cos\theta + \frac{\pi d^2}{4}\left(u_{nw} - u_w\right) \le \pi d T_s\cos\theta + \frac{\pi d^2 T_s}{\max\left(d_{th}\right)} \le 2\pi d T_s \ \ (for\ uniform\ grain\ size) \quad (17)$$

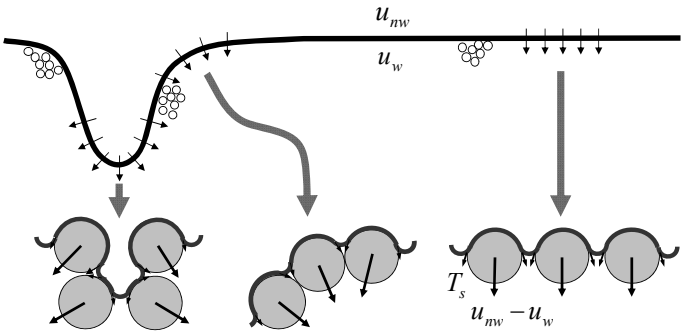

Figure 10. Forces on particles under mixed fluid flow condition (Shin & Santamarina 2010b).

Upscaling – grain models. Particle-scale forces determine the equilibrium of each particle and its eventual displacement. Sediment-scale implications can be explored using particle models, which are based on Newtonian mechanics. The resultant force F acting on a given particle of mass m causes it to accelerate with $a=F/m$. After a time interval Δt, the particle is at a new location $\Delta x=v_0\Delta t+at^2/2$ and experiences a new set of forces.

4 MACRO-SCALE PHENOMENA: MIXED FLUID FLOW

Pore-scale and particle-scale conditions identified in previous sections are used herein to explore important phenomena that take place in sediments in the context of energy geotechnology.

4.1 *Fluid invasion - Mixed fluid conditions*

Fluid invasion under mixed fluid conditions is controlled by capillary F_c, viscous drag F_d and weight/bouyancy W or F_b forces. These forces can be combined into dimensionless numbers (Pennel et al. 1996, Lenormand et al. 1988 – Note: the defending and invading fluid viscosities are μ_{def} and μ_{inv}):

$$N_C = \frac{F_d}{F_c} = \frac{3\pi d\mu_{inv}v}{\pi d T_s \cos\theta} = \frac{3\mu_{inv}v}{T_s\cos\theta} \tag{18}$$

$$N_M = \frac{\mu_{inv}}{\mu_{def}} \tag{19}$$

$$N_G = \frac{F_d}{W} = \frac{3\pi d\mu_{inv}v}{\pi G_s\gamma_w d^3/6} = \frac{18\mu_{inv}v}{G_s\gamma_w d^2} \tag{20}$$

$$N_B = \frac{F_b}{F_c} = \frac{\Delta\gamma\,\pi d^3/6}{\pi d T_s\cos\theta} = \frac{\Delta\gamma\, d^2}{6T_s\cos\theta} \tag{21}$$

Invasion conditions and emergent phenomena can be identified in the dimensionless space of these π-ratios. Figure 11 shows a 2D-slice of this space.

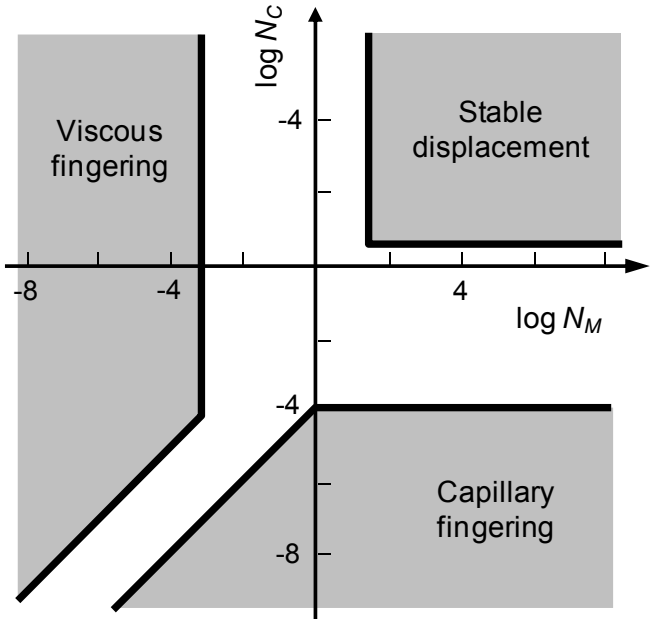

Figure 11. Space for viscous fingering, capillary fingering, and stable displacement in terms of dimensionless ratios N_M and N_C – refer to text (modified from Lenormand et al. 1988).

Conditions relevant to energy geotechnology are identified next:

- Water invades a dry sediment: slow, capillary driven invasion by a wetting fluid follows the connectivity among the smallest pores.
- Oil invades a water-saturated sediment: slow invasion by a non-wetting high viscosity fluid takes place by overcoming capillary resistance, i.e., invades largest pores first.
- Gas storage into a water saturated sediment and gas production during hydrate dissociation: invasion by a non-wetting low viscosity fluid.
- Liquid CO_2 is injected into a water saturated sediment: the non-wetting liquid CO_2 has a viscosity two orders of magnitude smaller than water (Jung et al. 2010). Viscous fingering may develop (high N_c and low N_m in Figure 11 – see Qi et al. 2009).
- Ice and hydrate growth: it resembles the slow invasion of a high viscosity non-wetting phase.

4.2 *Breakthrough pressure*

The long-term storage of CO_2 is a quasi-static condition controlled by capillary forces at pore throats. Similar conditions apply to gas and oil storage. The distribution of pore size discussed in Section 3.1 is invoked in this analysis. For a given pore structure, the breakthrough pressure p_c^* determined by the pressure-dependent interfacial tension T_s and contact angle θ is given by

$$p_c^* = \frac{4T_s\cos\theta}{d_p^*} \tag{22}$$

where d_p^* is the minimum pore diameter along a percolating path across the seal layer. The pore size

d_p^* can be related to the mean by a factor α of the standard deviation. For a log-normally distributed pore size,

$$\ln\left(\frac{d_p^*}{nm}\right) = \mu\left(\ln\frac{d_p}{nm}\right) + \alpha\sigma\left[\ln\left(\frac{R_p}{\mu m}\right)\right] \quad (23)$$

The analysis of gas breakthrough data in Hildenbrand et al. (2002), in Hildenbrand et al. (2004) and in Horseman et al. (1999) leads us to conclude that percolating paths are made of pores larger than the mean, and that the second term in Equation 23 is relatively independent of effective stress (Espinoza & Santamarina 2010). We note that this analysis does not take into consideration poro-mechanical effects (pore size is affected by the percolating immiscible fluid and the ensuing capillary forces – Section 4.6) and reactive fluid transport (which also affects the pore size along the percolating path – Section 4.9)

4.3 *Gas invasion -vs.- internal gas nucleation*

Expressions for degree of saturation and permeability as a function of capillary pressure have been derived for typical drying soil conditions where water vapor is in a continuous phase with the atmosphere. These Δu-S expressions can be used to investigate similar conditions in energy geotechnology, such as the injection of liquid CO_2 into water-saturated sediments. However, gas comes out of solution and bubbles grow within the sediment in various energy-related applications, from oil recovery to methane production from hydrate bearing sediments (as well as frequent seepage conditions downstream of earth dams). These two cases are referred to "internal gas drive process" for the case of nucleation and gas liberation during depressurization, and "external gas drive process" or gas injection for the case of forced invasion (Yortsos & Parlar 1989, Poulsen et al. 2001, Nyre et al., 2008).

We use 3D network models to explore the effect of gas invasion versus nucleation on the evolution of the characteristic saturation curves and relative permeabilities (details in Jang & Santamarina 2010c). We assume slow invasion and nucleation so that the process is controlled by capillary forces – both viscous and gravity forces are disregarded (refer to Section 4.1). Gas invasion is enforced from a peripheral gas-water interface, while gas nucleation is initiated at randomly selected internal nodes; the algorithm and tube size distribution are identical in both invasion and nucleation simulations. Results are described in terms of the defending fluid retention and relative permeabilities.

Characteristic curve in random media. The characteristic curve captures the causal link between water saturation and capillary pressure (See also Wilkinson & Willemsen 1983, Lenormand & Zarcone 1984). Pore throat size distribution and spatial correlation govern the shape of the characteristic curve (Francisca & Arduino 2007). The lower bound characteristic curve is determined by sorting pores and gradually invading from the largest pore to the smallest one; conversely, the upper bound is obtained by invading the smallest pore first and blasting through the sediment as gradually larger pores are invaded. Real cases fall in between these two extremes. The characteristic curves for spatially-uncorrelated random-distributed pores are shown in Figure 12a (Simulation details are indicated in the figure caption). Results are almost identical for gas invasion and gas nucleation. Water has been displaced in most tubes when the capillary pressure corresponds to the mean pore size, which in this case is Δu=0.14MPa for $\mu(R_{tube})$=1μm.

Relative permeabilities. Gas and water conductivity during gas invasion and nucleation are calculated at each saturation. Computed water conductivities are normalized by the water conductivity of the fully water saturated network (Figure 12b). Gas conductivities are normalized by the gas conductivity obtained when gas invasion process is completed. The normalized water conductivities are almost same for both gas invasion and nucleation.

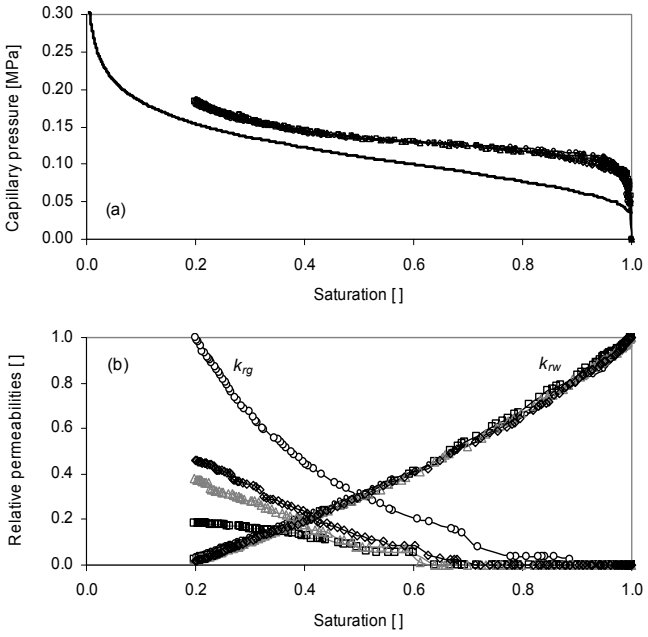

Figure 12. Characteristic curves and relative permeabilities - Gas invasion vs. gas nucleation. (a) Characteristic curves. Symbols: (○) gas invasion through 13^2 nodes on one side, (-) gas invasion into the network sorted by tube size; gas invasion through multiple nodes distributed inside network model: (□) 13^2, (Δ) 2×13^2, (◊) 3×13^2 nodes. (b) Relative conductivity of water k_{rw} and gas k_{rg}. Results obtained using a three dimensional tube-network model. Details: 13×13×13 nodes, 5460 tubes, coordination number cn=6, log-normal distribution of tube radius R, the mean tube size $\mu(R)$=1μm, and the standard deviation in tube radius σ(ln(R/[μm]))=0.4. Parameters for Young' equation $P_c=2T_{LV}\cos\theta/R$: T_{LV}=72 mN/m, θ=0°.

However, gas conductivity during nucleation is much lower than during gas invasion. Similar conclusions were reached by Poulsen et al. (2001) using different model characteristics.

Other implications. There are important porogranular mechanical distinctions between gas invasion and nucleation conditions. First, we observe that isolated bubbles can exist at different gas. Second, a capillary front evolving at the sediment boundary (e.g., during desiccating) tends to cause sediment compaction, while internal nucleation promotes expansion. These two cases are discussed later in this section, in the context of desiccation cracks and bubble migration.

4.4 *Residual saturation – recovery efficiency*

Oil recovery efficiency is controlled by pore connectivity and water invasion. The recovery of gas from hydrate bearing sediments depends on volume expansion upon dissociation.

Oil recovery. The displacement efficiency E_O during oil recovery can be defined in terms of the initial oil saturation S_{oi} and the residual oil saturation S_{or} as

$$E_O = \frac{S_{oi} - S_{or}}{S_{oi}} \tag{24}$$

Residual oil saturation after water flooding ranges from ~10% to ~40%, depending on the sediment heterogeneity and flooding conditions (Morrow 1990).

Gas hydrates. Internal gas nucleation and gas expansion creates conditions that are different to oil extraction. We use pore-network simulations to investigate gas recovery efficiency and residual gas saturation. An analytical result can also be obtained for gas recovery efficiency E_G using macro-scale analyses (details in Jang & Santamarina 2010b)

$$E_G = \frac{V_g^{rec}}{V_g^{dis}} = \frac{V_g^{dis} - V_g^{res}}{V_g^{dis}} = \frac{\beta V_h^{ini} - 0.79 V_h^{ini} - V_g^{res}}{\beta V_h^{ini} - 0.79 V_h^{ini}}$$

$$= \frac{\beta - 0.79 - S_g^{res} \big/ S_{hyd}}{\beta - 0.79} \quad (0.21 S_h \le S_g^{res} \le 1) \tag{25}$$

where the V_h^{ini} is initial hydrate volume and V_g^{res} is residual gas saturation per unit volume of sediment, S_{hyd} is initial hydrate saturation, β represents the expansion of dissociated gas and water from initial volume of hydrate. Numerical and analytical results presented in Figure 13.

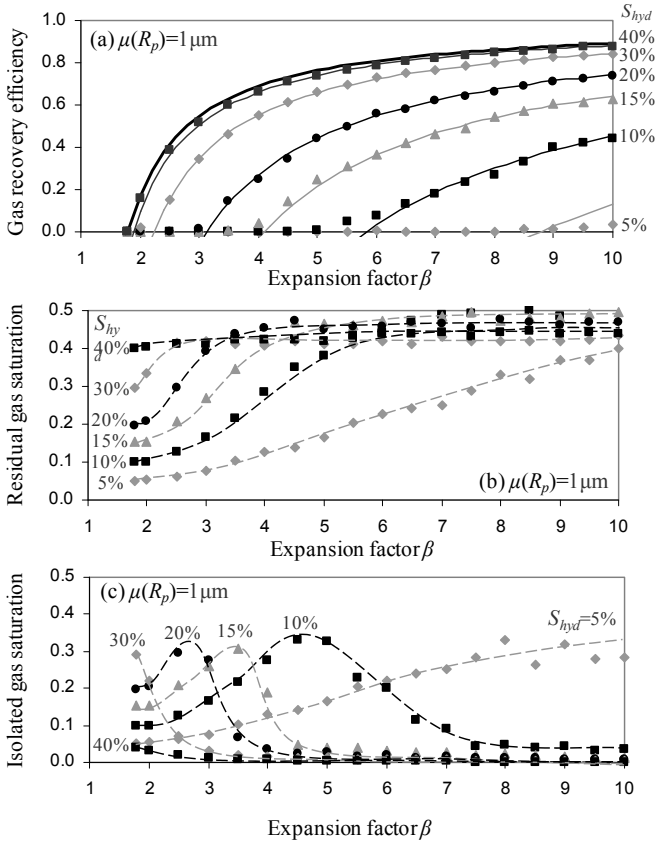

Figure 13. Gas production from hydrate bearing sediments. (a) Recovery efficiency. (b) Residual gas saturation. (c) Isolated gas saturation. Each point is an average of 20 realizations. Three-dimensional pore-network model: 15×15×15 pores. Randomly distributed pore radius with constant mean $\mu(R_p)$=1μm and standard deviation $\sigma[\ln(R_p)]$=0.4. Pore throat R_{th}=0.5·*min*(R_{p1}, R_{p2}). Periodic boundary condition is used. Parameters for Young' equation $P_c = 2T_{LV}\cos\theta/R$: T_{LV}=72mN/m, θ=0° (from Jang & Santamarina 2010b).

Results show that gas recovery efficiency and residual gas saturation during hydrate dissociation are functions of initial hydrate saturation, mean pore size, and the variability in pore size distribution.

5 MACRO-SCALE PHENOMENA: MECHANICAL EFFECTS

The ratio $F_c/N = 2\pi T_s/(\sigma' d)$ –refer to Table 5- defines two extreme regimes: mixed fluid conditions do not affect the mechanical behavior of the sediment if $F_c/N \ll 1$, conversely capillary phenomena will have a profound effect on the sediment mechanical response when $F_c/N \gg 1$ (Fig. 14). Clearly, this analysis can be extended to include other particle level forces, such as cementation and electrical attraction. Salient phenomena are discussed next.

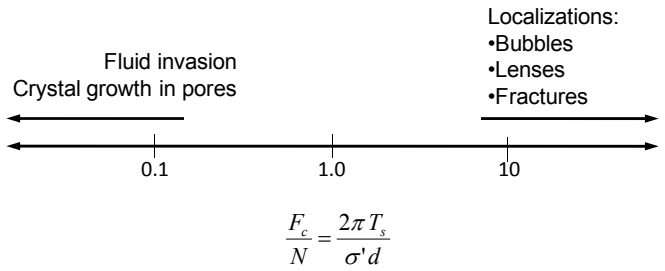

Figure 14. Capillary force vs. skeletal force. Localizations develop at high F_c/N ratio.

5.1 *Seepage and gas nucleation: bottom blow up*

Bubble nucleation during depressurization and associated changes in hydraulic conductivity may combine to create unwanted failure conditions (we acknowledge studies by Japanese researchers in the early 1990's). Consider upward flowing liquid through a soil plug of length H. The liquid pressure at the lower inlet is u_i, and u_o at the upper outlet. The liquid pressure when gas comes out of solution is the bubble point u_b (Note: the liquid is not gas saturated at pressure u_i).

Let's assume that equilibrium has been reached so that the continuity of water flow is maintained throughout the saturated and unsaturated soil layers $q_w(\text{sat})=q_w(\text{unsat})$, and that the hydraulic conductivities are related as $k_{unsat}=\alpha \cdot k_{sat}$ (Fig. 15).

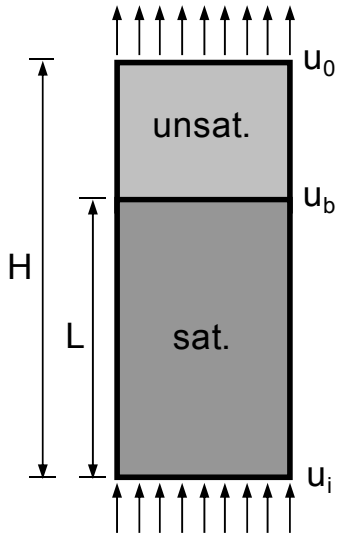

Figure 15. Gas dissolution, changes in permeability and the potential development of glow-up conditions.

Then, the elevation L where gas comes out of solution can be computed from the following quadratic equation in L (the explicit solution for L is not shown here)

$$q_w\big|_{sat} = q_w\big|_{unsat} \tag{26}$$

$$\frac{\left(\frac{u_i}{\gamma_\ell}\right)-\left(\frac{u_b}{\gamma_\ell}+L\right)}{L} = \alpha \frac{\left(\frac{u_b}{\gamma_\ell}+L\right)-\left(\frac{u_o}{\gamma_\ell}+H\right)}{H-L}$$

The hydraulic gradient is higher in the unsaturated zone, and uplift may cause blow up. The effective stress becomes zero at the elevation of the bubble point L when

$$u_i - u_b = L\left[\alpha\,\gamma_{tot} + (1-\alpha)\,\gamma_\ell\right] \approx L\left[(1+\alpha)\,\gamma_\ell\right] \tag{27}$$

5.2 *Development of discontinuities – granular mechanics effects*

Desiccation cracks - Immiscible fluid cracks. The fundamental particle-level mechanism for desiccation crack initiation and growth is centered on the air-water interface membrane. Initially the air-water interface membrane resists invading pores, capillary suction increases, the effective stress increases, the soil consolidates, and the skeletal stiffness increases. Eventually, the air-water interface membrane invades the largest pores and causes particle displacement away from the invasion point. The void ratio increases at the tip and facilitates further membrane invasion and crack growth (Fig. 10 & 16). The same mechanism is responsible for fluid-driven fractures when other immiscible fluids are involved, such as gas-oil, gas-water, and oil-water systems.

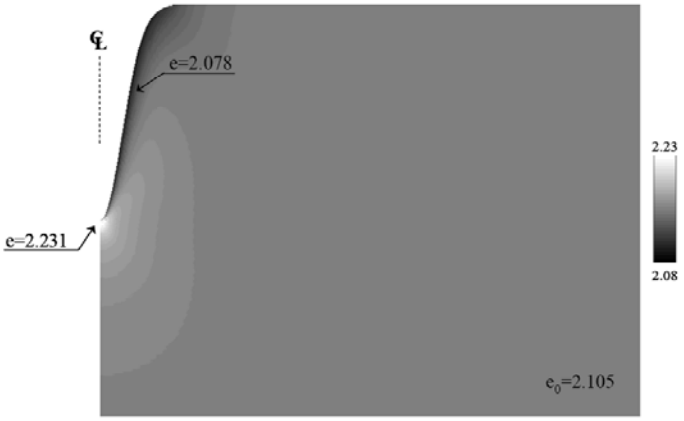

Figure 16. Surface defects and crack initiation. Local void ratio evolution during desiccation (Shin & Santamarina 2010a).

Ice and hydrate lenses. The formation of segregated ice and hydrate lenses responds to similar force-balance conditions and the granular-mechanics effects at the tip: lens growth causes an increase in porosity at the tip, fluid migrate toward the tip and further nucleation is favored.

The growth of ice lenses is temperature controlled, and they typically develop parallel to the soil surface in frozen ground due to the advancing cold front, that is normal to the σ_1'-direction (see Gens 2010). However, hydrate growth is gas-limited in most cases; in other words, sediments are already within the *P-T* stability field and hydrate grows as methane becomes available. In this case, hydrate lens growth is facilitated normal to the minor principal stress σ_3' (evidence in Yun 2005).

Localization regime. As the particle size decreases, the particle weight and the skeletal force decrease faster than either the capillary force and the force exerted by the ice or hydrate lens. Hence, fine-grained soils are more susceptible to fluid-driven fractures and lens formation (Fig. 17 – see also Jain & Juanes 2009).

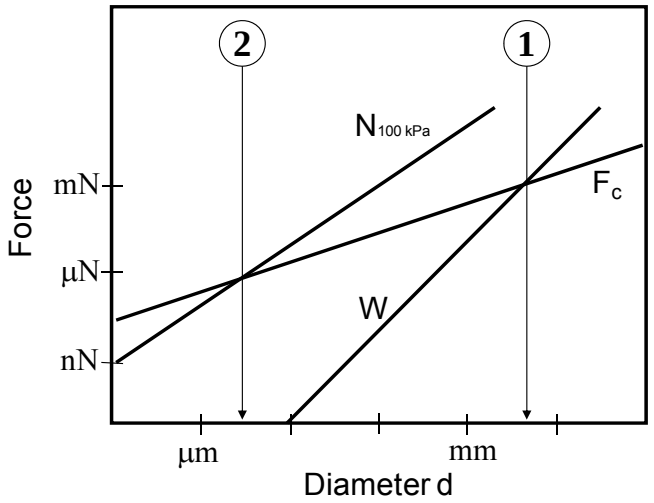

Figure 17. Skeletal force, capillary force, and weight of particles of different size (from Santamarina 2001).

5.3 *Buoyancy and bubble migration*

Bubbles larger than the critical size of nuclei $d>d^*$ can coalesce to form even larger bubbles. These large bubbles become trapped at pore throats defining Laplacian capillary surfaces. As the bubble size increases, so does the buoyancy drive and its tendency to migrate upwards (experimental evidence in Boudreau et al. 2009).

Buoyancy drive applies to other light and immiscible fluids. Consider a gas bubble that extends from depth z to depth $z + L$, composed of a gas of unit weight much lower than the unit weight of water $\gamma_g << \gamma_w$. If the capillary pressure at the bottom of the bubble is Δu^{bottom}, the capillary pressure at the top is equal to $\Delta u^{top} = \Delta u^{bottom} + L\gamma_w$ (Fig. 18).

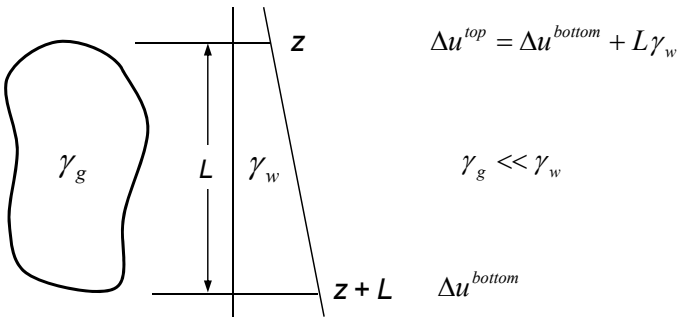

Figure 18. Elongated gas bubble subjected to different capillary pressure in saturated sediments.

On the other hand, the effective stress increases with depth, $\sigma'(z) < \sigma'(z + L)$ and both porosity and pore size decrease with depth (Eq. 12). Large capillary pressure and pore size at shallower depths explain the upwards propagate of bubbles The analysis can be extended to other immiscible buoyant fluids.

Other observations are anticipated: (1) migrating bubbles coalesce with other bubbles found along their trajectory; coalescence and lower water pressure towards the surface lead to marked bubble expansion as the bubble approaches the sediment surface; (2) thinner bubbles will develop in sediments of higher stiffness; (3) long tubular bubbles cause higher capillary pressure for the same gas volume and may favor propagation in strong sediments; (4) a continuous bubble may not connect the source to the free sediment surface: discontinuous bubbles are needed to build up gas pressure. Therefore, gas bubble migration through sediments is inherently intermittent.

5.4 *Monitoring: bulk stiffness*

The monitoring of energy related processes is often conducted with *P*-wave propagation techniques. The stiffness of small bubbles has to be given special attention.

Bubbles much smaller than soil particles can fit within the pore space without distorting the soil structure. Thus, the presence of gas bubbles only changes the compressibility of the pore fluid (Wheeler 1988). Even relatively small size bubbles are sufficient to significantly change the pore fluid bulk stiffness (Sparks 1963, Santamarina et al. 2001). The pore fluid bulk stiffness κ_f depends on the degree of saturation S, the bulk stiffness of water κ_w (~2.2GPa) and the bulk stiffness of gas bubbles κ_b. The bulk stiffness of bubbles is intimately related to the gas pressure, which is governed by the surface tension and the bubble size d_b. We can show that (Rebata-Landa & Santamarina 2010):

$$\kappa_b = \frac{4T_s}{3d_b} \tag{28}$$

Then, the fluid bulk stiffness of water becomes:

$$\kappa_f = \frac{1}{S\dfrac{1}{\kappa_w} + (1-S)\dfrac{3d_b}{4T_s}} \tag{29}$$

Finally, the bulk stiffness of sediments in the presence of disseminated gas bubbles is:

$$\kappa_{soil} = \kappa_{sk} + \frac{1}{n\left[S\dfrac{1}{\kappa_w} + (1-S)\dfrac{3d_b}{4T_s}\right] + \dfrac{1-n}{\kappa_g}} \tag{30}$$

In laboratory and field applications, the global bulk stiffness of the soil κ_{soil} and its skeletal stiffnes κ_{sk} can be inferred from S-wave velocity measurements

5.5 *Reactive fluid transport*

Fluids react with the mineral walls and alter the sediment structure. Consider carbon dioxide: CO_2 dissolves in water to form carbonic acid H_2CO_3, which eventually ionizes into H^+ and CO_3^{2-} lowering the pH of water. Minerals dissolve in acid water with dissolution rates that are proportional to the pH difference with respect to the buffer pH. The solubility of CO_2 increases with pressure (Stumm & Morgan 1996). Conversely, a reduction in pressure produces the nucleation of CO_2 gas and the precipitation of dissolved minerals. Therefore, both dissolution and re-precipitation can take place in the sediment.

Mineral dissolution in the pore fluid satisfies similar concepts to those discussed in Section 2.4, albeit the low saturation concentration. Mineral dissolution by acidic water flow is most relevant to long-term geological storage of CO_2. Similar situations apply to other energy geotechnology systems including hydrate dissolution by unsaturated water flow. Three potential emergent phenomena are discussed next.

Dissolution pipes (Hydro-chemical coupling). A positive feedback condition develops between dissolution and preferential fluid flow paths. Eventually, high conductivity flow channels or "wormholes" may emerge (Hoefner & Fogler 1988; Fredd & Fogler 1998). Damköhler's number D_a= dissolution rate / advective transport rate, and Peclet's number P_e= advective transport rate / diffusion transport rate are used to explore the phenomenon: wormholes form at high P_e>1 and D_a>1 numbers (Golfier et al. 2002).

Change in capillary forces (mixed-fluid skeleton coupling). Pore size enlargement during mineral dissolution or pore size reduction during precipitation alters capillary forces when immiscible fluids are involved.

Change in internal skeletal stresses (chemo-mechanical coupling). Mineral dissolution produces a pronounced drop in horizontal effective stress under zero lateral strain conditions. The state of stress decreases from a k_o-state and reaches the active shear failure k_a-state after ~5% mineral dissolution (Shin & Santamarina 2009). Furthermore, shear localization may take place during mineral dissolution in sediments that exhibit postpeak strain softening behavior (in agreement with Rudnicki & Rice 1975 - Details in Shin et al. 2008).

6 CONCLUSIONS

Problems related to energy geotechnology often involve mixed-fluid conditions. However, contrary to near-surface unsaturated soil mechanics, most energy geotechnology problems are at high fluid pressure and in deep sediments. This leads to phenomena seldom encountered in the more classical unsaturated soil literature. Processes reviewed in this manuscript are relevant to oil and gas, hydrate bearing sediments and carbon geological storage. The most important observations follow.

- Surface tension is pressure-dependent. Contact angle is determined by the interfacial tension of neighboring phases, thus, it is pressure dependent as well.
- Capillary phenomena can be extended to include ice and hydrates. While the phase boundary for ice is almost constant with pressure, the stability field for hydrates is pressure and temperature dependent.
- Solubility is pressure and temperature dependent, and it is affected by the presence of other phase or solutes. Supersaturation facilitates nucleation. The higher saturation around smaller nuclei leads to diffusion-controlled ripening.
- Ice formation and melting is accompanied by volume change and affects the granular skeleton. Volume change is much more pronounced when gas hydrates are involved.
- The nucleation of a gas phase in pores reduces the sediment bulk stiffness, alters the hydraulic conductivity, and may lead to a zero effective stress condition, as observed in bottom blowup situations.
- Capillary pressure is a function of interfacial tension and curvature, and is related to relative humidity (water-vapor) or temperature (ice or hydrate). Hence, the size of pores invaded by the non-wetting phase can be related to relative humidity (vapor) or temperature (ice and hydrate).
- Pore size distribution and spatial connectivity govern fluid flow, percolation, break-through pressure, residual saturation and resource recovery efficiency. The percolating path for an immiscible fluid is made up of pores within the upper-side tail of the pore size distribution.
- The characteristic saturation curves Δu-S show no significant difference for gas invasion and gas nucleation, and there is almost no difference for liquid relative permeability in these two cases. However, the gas relative permeability is lower for internal gas nucleation compared to gas invasion.
- Particle size distribution determines pore size and particle-level forces, which eventually define the sediment response. Forces are of gravitational, skeletal (related to effective stress), viscous, capillary, and electrical origin. These forces can be combined

into dimensionless ratios to facilitate the identification of physical regimes and emergent phenomena.

- Pore size changes as immiscible fluids cause particle-level capillary forces and particle displacement. Immiscible fluid-driven fractures, desiccation cracks, and gas bubble migration reflect these particle-scale mechanisms.
- The invading fluid may react with minerals. Reactive fluid transport alters the sediment structure, induces localized flow, forms high conductivity flow channel, and changes skeletal stresses. Storativity and the performance of seal layers is limited by these emergent phenomena.

Acknowledgements. Support for this research has been provided by the Department of Energy, the National Science Foundation and the Goizueta Foundation. We are grateful to A. Sivaram for proofreading the manuscript.

NOTATION

c	Solute concentration	[mol/L]
C_c	Compressibility coefficient	[ ]
d	Particle diameter	[m]
d_b	Bubble diameter	[m]
d_p	Pore diameter	[m]
d^*	Critical nuclei size	[m]
d_p^*	Minimum pore diameter	[m]
d_{th}	Throat diameter	[m]
D_a	Damköhler's number	
e	Void ratio	[ ]
E_G	Gas recovery efficiency	[ ]
E_O	Oil recovery efficiency	[ ]
F_{cap}	Capillary force	[N]
k_H^0	Henry's constants	[M/atm]
M	Molecular weight	[g/mol]
$M_{P,T}$	Solubility	[mol/m^3]
N	Normal contact force	[N]
n	Porosity	[ ]
P_{c_*}	Capillary pressure	[N/m^2]
p_c^*	Breakthrough pressure	[N/m^2]
P_e	Peclet's number	
q	Flow rate	[m^3/s]
r	Gas bubble radius	[m]
$\underline{R}$	Gas constant $\underline{R}$=8.31 N·m/(mol·K)	
R_{tube}	Tube radius	[m]
S	Saturation	[ ]
S_g^{res}	Residual gas saturation	[ ]
S_{hyd}	Hydrate saturation	[ ]
S_{oi}	Initial oil saturation	[ ]
S_{or}	Residual oil saturation	[ ]
T	Temperature	[K]
T_{LV}	Interfacial tension liquid-vapor	[mN/m]
T_{LV}	Interfacial tension liquid-vapor	[mN/m]
T_m	Melting temperature	[K]
T_s	Interfacial tension	[mN/m]
T_{VS}	Interfacial tension vapor-solid	[mN/m]
u_L	Liquid pressure	[N/m^2]
u_V	Vapor pressure	[N/m^2]
V_g^{dis}	Dissociated gas volume	[m^3]
V_g^{rec}	Recovered gas volume	[m^3]
V_g^{res}	Residual gas volume	[m^3]
V_h^{ini}	Initial hydrate volume	[m^3]
β	Fluid expansion factor	[ ]
γ	Solute activity coefficient	[ ]
γ_f	Unit weight of fluid	[N/m^3]
γ_g	Unit weight of gas	[N/m^3]
γ_m	Unit weight of mineral	[N/m^3]
γ_w	Unit weight of water	[N/m^3]
δ	Degree of supersaturation	[ ]
ΔH	Enthalpy of solution	[J/mol]
θ	Contact angle	[°]
κ_b	Bulk stiffness of gas bubble	[GPa]
κ_f	Bulk stiffness of pore fluid	[GPa]
κ_g	Bulk stiffness of soil particle	[GPa]
κ_{sk}	Sulk stiffness of soil skeletal	[GPa]
κ_{soil}	Sulk stiffness of soil	[GPa]
κ_w	Bulk stiffness of water	[GPa]
Γ	Surface excess of solute	[mol/m^2]
μ	Viscosity	[N·s/m^2]
ρ	Density	[kg/m^3]
σ'	Effective stress	[N/m^2]
Σ_m	Melting entropy	[MPa/K]

REFERENCES

Adamson, A.W. & Gast, A.P. 1997. *Physical chemistry of surfaces*. 6th Ed., New York: Wiley.

Anderson, R., Llamedo, M., Tohidi, B., & Burgass, R.W. 2003. Experimental measurement of methane and carbon dioxide clathrate hydrate equilibria in mesoporous silica, *J. of physical chemistry B*. 107: 3507-3514.

Bauer, B.A. & Patel, S. 2009. Properties of water along the liquid-vapor coexistence curve via molecular dynamics simulations using the polarizable TIP4P-QDP-LJ water model. *The J. of chemical physics* 131: 084709-1:16

Bhatt, D., Newman, J., & Radke, C.J. 2004. Molecular dynamics simulations of surface tensions of aqueous electrolytic solutions. *J. of physical chemistry B*. 108: 9077-9084.

Blander, M. 1979. Bubble nucleation in liquids. *Advances in colloid and interface science*. 10: 1-32.

Blunt, M.J. 2001. Flow in porous media – pore-network models and multiphase flow. *Current opinion in colloid & interface science*. 6: 197-207.

Boudreau, B.P., Algar, C., Johnson, B.D., Croudace, I., Reed, A., Furukawa, Y., Dorgan, K.E., Jumars, P.A., Grader, A.S., & Gardiner, B.S. 2009. Bubble growth and rise in soft sediments, *Geology*, 33: 517-520.

Butt, H.-J., Graf, K., & Kappl, M. 2006. *Physics and chemistry of interface*. 2nd Ed. Weinheim: Wiley-VCH Verlag GmbH & Co. KGaA.

Chi, S.-M., Morsi, B.I., Klinzing, G.E., & Chiang, S.-H. 1988. Study of interfacial properties in the liquid CO_2-water-coal system. *Energy & Fuels*. 2: 141-145.

Chiquet, P., Broseta, D., & Thibeau, S. 2007. Wettability alteration of caprock minerals by carbon dioxide. *Geofluids*. 7: 112-122.

Cho, G.C. & Santamarina, J.C. 2001. Unsaturated particulate materials – Particle-level studies. *J. of geotechnical and geoenvironmental engineering*. 127: 84-96.

Chun, B.-S. & Wilkinson, G.T. 1995. Interfacial tension in high-pressure carbon dioxide mixtures. *Industrial & engineering chemistry research*. 34: 4371-4377.

Clennell, M.B., Hovland, M., Booth, J.S., Henry, P., & Winters, W.J. 1999. Formation of natural gas hydrates in marine sediments 1. Conceptual model of gas hydrate growth conditioned by host sediment properties. *J. of geophysical research*. 104: 22985-23003.

Coussy, O. 2005. Poromechanics of freezing materials. *J. of the mechanics and physics of solids*, 53: 1689-1718.

Coussy, O. & Monteiro, P. 2007. Unsaturated poroelasticity for crystallization in pores. *Computers and geotechnics*, 34: 279-290.

da Rocha, S.R.P., Johnston, K.P., Westacott, R.E., & Rossky, P.J. 2001. Molecular structure of the water–supercritical CO_2 interface. *J. of physical chemistry B*. 105: 12092-12104.

Davie, M.K., Zatsepina, O.Y., & Buffett, B.A. 2004. Methane solubility in marine hydrate environments. *Marine geology*. 230: 177-184.

Defay, R. & Prigogine, I. 1966. *Surface tension and adsorption*. New York: John Wiley & Sons.

Dickson, J.L., Gupta, G., Horozov, T.S., Binks, B.P., & Johnson, K.P. 2006. Wetting phenomena at the CO_2/water/glass interface. *Langmuir*. 22: 2161-2170.

Dominguez, A., Bories, S., & Prat, M. 2000. Gas cluster growth by solute diffusion in porous media. Experiments and automation simulation on pore network. *International J. of multiphase flow*. 26: 1951-1979.

Dullien, F.A.L. 1992, *Porous media fluid transport and pore structure*, 2nd Ed. New York: Academic.

Espinoza, D.N. & Santamarina, J.C. 2010. Water-CO_2-mineral systems: interfacial tension, contact angle and diffusion–Implications to CO_2 geological storage. *Water resources research*. Accepted for publication.

Extrand, C.W. 1998. A thermodynamic model for contact angle hysteresis. *J. of colloid and interface science*. 207: 11-19.

Finkelstein, Y. & Tamir, A. 1985. Formation of gas bubbles in supersaturated solutions of gases in water. *American institute of chemical engineers J.*. 31: 1409-1419.

Francisca, F.M. & Arduino, P. 2007. Immiscible displacement model for anisotropic and correlated porous media. *International J. of geomechancis*. 7: 311-317.

Francisca, F.M., Rinaldi, V.A., & Santamarina, J.C. 2003. Instability of hydrocarbon films over mineral surfaces: Microscale experimental studies. *J. of environmental engineering*. 120: 1120-1128.

Fredd, C.N. & Fogler, H.S. 1998. Influence of transport and reaction on wormhole formation in porous media. *American institute of chemical engineers J.*. 44: 1933-1949.

Gens, A. 2010. Soil-environment interactions in geotechnical engineering, *Géotechnique*. 60: 3-74.

Gerth, W.A. & Hemmingsen, E.A. 1980. Heterogeneous nucleation of bubbles at solid surfaces in gas-supersaturated aqueous solutions. *J. of colloid and interface science*. 74: 80-89.

Gili, J.A. & Alonso, E.E. 2002. Microstructural deformation mechanisms of unsaturated granular soils, *International J. for numerical and analytical methods in geomechanics*, 26 : 433-468.

Golfier, F., Zarcone, C., Bazin, B., Lenormand, R., Lasseux, D., & Quintard, M. 2002. On the ability of a Darcy-scale model to capture wormhole formation during the dissolution of a porous medium, *J. of fluid mechanics*, 457 : 213-254.

Hemmingsen, E.A. 1975. Cavitation in gas-supersaturated solutions. *J. of applied physics*. 46: 213-218.

Hemmingsen, F.A. 1977. Spontaneous formation of bubbles in gas-supersaturated water. *Nature*. 267: 141-142.

Henry, P., Thomas, M., & Clennell, M.B. 1999. Formation of natural gas hydrates in marine sediments 2. Thermodynamic calculations of stability conditions in porous sediments. *J. of geophysical research*. 104: 23005-23022.

Hildenbrand, A., Schlomer, S., & Krooss, B.M. 2002. Gas breakthrough experiments on fine-grained sedimentary rocks. *Geofluids*. 2: 3-23.

Hildernbrand, A., Schlomer, S., Krooss, B.M., & Littke, R. 2004. Gas breakthrough experiments on politic rocks: comparative study with N_2, CO_2 and CH_4. *Geofluids*. 4: 61-80.

Hoefner, M.L. & Fogler, H.S. 1988. Pore evolution and channel formation during flow and reaction in porous media. *American institute of chemical engineers J.*. 34: 45-54.

Horseman, S.T., Harrington, J.F., & Sellin, P. 1999. Gas migration in clay barriers. *Engineering geology*. 54: 139-149.

Jain A.K. & Juanes R. 2009, Preferential Mode of gas invasion in sediments: Grain-scale mechanistic model of coupled multiphase fluid flow and sediment mechanics, *J. of geophysical research*, 114: B08101.

Jang, J. & Santamarina, J.C. 2010a. Hydraulic conductivity in spatially varying media – A pore-scale investigation. *Geophysical J. international*. Under review.

Jang, J. & Santamarina, J.C. 2010b. Gas production from hydrate bearing sediments: Pore-network model simulation and macro-scale analyses. In preparation.

Jang, J. & Santamarina, J.C. 2010c. Evolution of water and gas saturation and relative permeabilities during gas invasion and gas nucleation. In preparation.

Jung, J.W., Espinoza, D.N., & Santamarina, J.C. 2010. Properties and phenomena relevant to CH_4-CO_2 replacement in hydrate bearing sediments. *J. of geophysical research*. Under review.

Kim, H. & Burgess, D. 2001. Prediction of interfacial tension between oil mixtures and water. *J. of colloid and interface science*. 241: 509-513.

Knight, C.A. 1971. Experiments on the contact angle of water on ice. *Philosophical magazine*. 23: 153-165.

Kuznetsova, T. & Kvamme, B. 2002. Thermodynamic properties and interfacial tension of a model water-carbon dioxide system. *Physical chemistry chemical physics*. 4: 937-941.

Kvamme, B., Kuznetsova, T., Hebach, A., Oberhof, A., & Lunde, E. 2007. Measurements and modelling of interfacial tension for water+carbon dioxide systems at elevated pressure. *Computational material science*. 38: 506-513.

Kwok, D.Y. & Neumann, A.W. 1999. Contact angle measurement and contact angle interpretation. *Advances in colloid and interface science*. 81: 167-249.

Kwon, T.-H., Cho, G.-C., & Santamarina, J.C. 2008. Gas hydrate dissociation in sediments: Pressure-temperature evolution. *Geochemistry Geophysics Geosystems*. 9: Q03019, doi:10.1029/2007GC001920

La Mer, V.K. 1952. Nucleation in phase transitions. *Industrial and engineering chemistry*. 44: 1270-1277.

Lenormand, R, touboul, E., & Zarcone, C. 1988. Numerical models and experiments on immiscible displacements in porous media. *J. of fluid mechanics*, 189: 165-187

Lenormand, R. & Zarcone, C. 1985. Invasion percolation in an etched network: measurement of a fractal dimension. *Physical review letters*. 54: 2226-2229.

Lubetkin, S.D. 2003. Why is it much easier to nucleate gas bubbles than theory predicts? *Langmuir*. 19: 2575-2587.

Massoudi, R. & King, A.D. 1974. Effect of pressure on the surface tension of water. Adsorption of low molecular weight gases on water at 25°C. *The J. of physical chemistry*. 78: 2262-2266.

Morrow, N.R. 1990. Wettability and its effect on oil recovery. *J. of petroleum technology*. 42: 1476-1484.

Myerson, A.S. 2002. *Handbook of industrial crystallization*, 2nd Ed. Boston: Butterworth-Heinemann.

Nyre, A.N., McDougall, S.R., & Skauge, A. 2008. Effect of depressurization on trapped saturations and fluid flow functions. *Improved oil recovery symposium*. SPE 113394. Tulsa, Oklahoma, 19-23 April.

Nývlt, J., Sohnel, O., Matuchova, M., & Broul, M. 1985. *The kinetics of industrial crystallization*. Amsterdam: Elsevier.

Pease, D.C. & Blinks, L.R. 1947. Cavitation from solid surfaces in the absence of gas nuclei. *J. of physical and colloid chemistry*. 51: 556-567.

Pegram, L.M. & Record, M.T. 2007. Hofmeister salt effects on surface tension arise from partitioning of anions and cations between bulk water and the air-water interface. *J. of physical chemistry B*. 111: 5411-5417.

Pennell, K.D., Pope, G.A., and Abriola, L.M. 1996. Influence of viscous and buoyancy forces on the mobilization of residual tetrachloroethylene during surfactant flushing. *Environmental science technology*, 30: 1328-1335.

Phadnis, H.S. & Santamarina, J.C. 2010. Pore size limited lift in sediments. In preparation.

Poulsen, S., McDougall, S.R., Sorbie, K.S., & Skauge, A. 2001. Network modeling of internal and external gas drive. *Proceeding of the 2001 International symposium of the society of core analysts (SCA)*. Edinburgh. Sept.

Qi, R., LaForce, T.C. & Blunt M.J. (2009), A three-phase four-component streamline-based simulator to study carbon dioxide storage, *Computational Geosciences*, *13*(4), 493-509

Rebata-Landa, V. & Santamarina, J.C. 2010. Biogenic gas bubbles in soils: Skempton's B parameter, P-wave velocity and liquefaction resistance. *J. of geotechnical and geoenvironmental engineering.* In print.

Ren, Q.-Y., Chen, G.-J., Yan, W., & Guo, T.-M. 2000. Interfacial tension of (CO_2+CH_4)+water from 298K to 373K and pressures up to 30MPa. *J. of chemical and engineering data*. 45: 610-612.

Ronen, D., Berkowitz, B., & Magaritz, M. 1989. The development and influence of gas bubbles in phreatic aquifers under natural flow conditions. *Trans in porous media*. 4: 295-306.

Rudnicki, J.W. & Rice, J.R. 1975. Conditions for the localization of deformation in pressure-sensitive dilatant materials. *J. of the mechanics and physics of solids*. 23: 371-394.

Santamarina, J.C. 2001. Soil behavior at the microscale: particle forces, *Proceedings of symposium of soil behavior and soft ground construction*, October, MIT.

Santamarina, J.C. & Jang, J. 2009. Gas production from hydrate bearing sediments: Geomechanical implication, NETL methane hydrate newsletter: *Fire in the Ice*. 9: 18-22. (http://www.netl.doe.gov).

Santamarina, J.C., Klein, K.A., & Fam, M.A. 2001. *Soils and waves*. London: John Wiley.

Shaw, D.J. 1992. *Introduction to colloid & surface chemistry*, 4th Ed. London: Butterworth-Heinemann.

Shin, H. & Santamarina, J.C. 2009. Mineral dissolution and the evolution of k_0. *J. of geotechnical and geoenvironmental engineering*. 135: 1141-1147.

Shin, H. & Santamarina, J.C. 2010a. Desiccation cracks in saturated fine-grained soils: particle level phenomena and effective stress analysis. *Geotechnique*. Under review.

Shin, H. & Santamarina, J.C. 2010b. Fluid-driven fractures in uncemented sediments: Underlying particle-level processes. *Earth and plenatary science letters*. Under review.

Shin, H., Santamarina, J.C., & Cartwright, J.A. 2008. Contraction-driven shear failure in compacting uncemented sediments. *Geology*. 36: 931-934.

Siemons, N., Bruining, H., Castelijns, H., & Wolf, K.-H. 2006. Pressure dependence of the contact angle in a CO_2-H_2O-coal system. *J colloid and interface science*. 297: 755-761.

Sloan, E.D. & Koh, C.A. 2008. *Clathrate hydrates of natural gases*, 3rd Ed. Boca Raton: CRC Press.

Sparks, A.D.W. 1963. Theoretical considerations of stress equations for partly saturated soils, *Third regional conference for Africa on soil mechanics and foundation engineering*. Salisbury. Rhodesia. 2-9 June. 215-218.

Stumm, W. & Morgan, J.J. 1996. *Aquatic chemistry: chemical equilibria and rates in natural waters*, 3rd Ed. New York: John Wiley & Sons.

Sun, R. & Duan, Z. 2007. An accurate model to predict the thermodynamic stability of methane hydrate and methane solubility in marine environments. *Chemical geology*. 244: 248-262

Sutjiadi-Sia, Y., Marckmann, H., Eggers, R., Holzknecht, C., & Kabelac, S. (2007), The effect of in liquids dissolved dense gases on interfacial and wetting characteristics, Forschung im Ingenieurwesen, 71, 29-45.

Sutjiadi-Sia, Y., Jaeger, P., & Eggers, R. 2008. Interfacial tension of solid materials against dense carbon dioxide. *J. of colloid and interface science*. 320: 268-274.

Tishchenko, P., Hensen, C., Wallmann, K., & Won, C.S. 2005. Calculation of the stability and solubility of methane hydrate in seawater. *Chemical geology*. 219: 37-52.

Treiber, L.E., Archer, D.L., & Owens, W.W. 1972. A laboratory evaluation of the wettability of fifty oil-producing reservoirs. *Society of petroleum engineers J.*. 12: 531-540.

Tuckermann, R. 2007. Surface tension of aqueous solutions of water-soluble organic and inorganic compounds. *Atmospheric environment*. 41: 6265-6275.

Uchida, T., Ebinuma, T., & Ishizaki, T. 1999. Dissociation condition measurements of methane hydrate in confined small pores of porous glass, *J. of physical chemistry* B. 103: 3659-3662

van Oss, C.J., Docoslis, A., & Giese, R.F. 2002. Role of the water-air interface in determining the surface tension of aqueous solutions of sugars, polysaccharides, proteins and surfactants, in *Contact angle, wettability and adhesion*, Volume 2, 3-12.

Waite, W.F., Santamarina, J.C., Corte, D.D., Dugan, B., Espinoza, D.N., Germaine, J., Jang, J., Jung, J.W., Kneafsey, T.J., Shin, H., Soga, K., Winters, W.J., & Yun, T.-S. 2009. Physical properties of hydrate-bearing sediment. *Reviews of geophysics*. 47: RG4003, doi:10.1029/2008RG00279.

Walsh, M.R., Koh, C.A., Sloan, E.D., Sum, A.K., & Wu, D.T. 2009. Microsecond simulations of spontaneous methane hydrate nucleation and growth. *Science*. 326: 1095-1098.

Ward, C.A., Balakris, A., & Hooper, F.C. 1970. On thermodynamics of nucleation in weak gas-liquid solutions. *J. of basic engineering – Transactions of the ASME*. 92: 695-704

Wheeler, S.J. 1988. A conceptual model for soils containing larger gas bubbles. *Geotechnique*. 38: 389-397.

Wilhelm, E., Battino, R., & Wilcock, R.J. 1977. Low-pressure solubility of gases in liquid water. *Chemical reviews*. 77: 219-262.

Wilkinson, D. & Willemsen, J.F. 1983. Invasion percolation: a new form of percolation theory. *J. of physics A: Mathematical and general*. 16: 3365-3376.

Yortsos, Y.C. & Parlar, M. 1989. Phase change in binary systems in porous media: application to solution-gas drive. *Society of petroleum engineers*. SPE 19697.

Yun, T.-S. 2005. Mechanical and thermal study of hydrate bearing sediments. Ph.D. thesis. Georgia Tech.

Zatsepina, O.Y. & Buffett, B.A. 1998. Thermodynamic conditions for the stability of gas hydrate in the seafloor. *J. of geophysical research*. 103: 24127-24139.